

Article

Atmospheric Air Plasma Treated SnS Films: An Efficient Electrocatalyst for HER

Po-Chia Huang ¹, Sanjaya Brahma ¹, Po-Yen Liu ¹, Jow-Lay Huang ^{1,2,3}, Sheng-Chang Wang ^{4,*}, Shao-Chieh Weng ¹ and Muhammad Omar Shaikh ⁴

¹ Department of Materials Science and Engineering, National Cheng Kung University, Tainan 70101, Taiwan; ma01a206@stust.edu.tw (P.-C.H.); Sanjayaphysics@gmail.com (S.B.); jacky199708@yahoo.com.tw (P.-Y.L.); J LH888@mail.ncku.edu.tw (J.-L.H.); jei1987@gmail.com (S.-C.W.)

² Center for Micro/Nano Science and Technology, National Cheng Kung University, Tainan 70101, Taiwan

³ Hierarchical Green-Energy Materials (Hi-GEM) Research Center, National Cheng Kung University, Tainan 70101, Taiwan

⁴ Department of Mechanical Engineering, Southern Taiwan University of Science and Technology, Tainan 710, Taiwan; omar.offgridsolutions@gmail.com

* Correspondence: scwang@stust.edu.tw; Tel.: +886-6-2533131 (ext. 3548); Fax: +886-6-2425092

Received: 10 September 2018; Accepted: 15 October 2018; Published: 17 October 2018



Abstract: Here, we demonstrate the enhanced water-splitting performance ($I = 10 \text{ mA/cm}^2$, Tafel slope = 60 mV/dec, onset potential = -80 mV) of atmospheric air plasma treated (AAPT) SnS thin films by the hydrogen evolution reaction (HER). The as prepared SnS films were subjected to Atmospheric Air Plasma Treatment (AAPT) which leads to formation of additional phases of Sn and SnO₂ at plasma powers of 150 W and 250 W, respectively. The AAPT treatment at 150 W leads to the evaporation of the S atoms as SO₂ generates a number of S-vacancies and Sn active edge sites over the surface of the SnS thin film. S-vacancies also create Sn active edge sites, surface p-type pinning that tunes the suitable band positions, and a hydrophilic surface which is beneficial for hydrogen adsorption/desorption. At high plasma power (250 W), the surface of the SnS films becomes oxidized and degrades the HER performance. These results demonstrate that AAPT (150 W) is capable of improving the HER performance of SnS thin films and our results indicate that SnS thin films can work as efficient electrocatalysts for HER.

Keywords: hydrogen evolution reaction; SnS; electrocatalysts; atmospheric air plasma treated

1. Introduction

Hydrogen evolution through the water splitting reaction has been proposed as a clean, efficient energy resource with zero emissions through an environmentally-friendly process. Recently, much effort has been undertaken towards the development of electrocatalytic/photocatalytic techniques to produce hydrogen efficiently through the hydrogen evolution reaction (HER) [1,2]. HER is a reduction reaction on the cathode surface via the adsorption of hydrogen ions that combine with an electron to form hydrogen gas ($2\text{H}^+ + 2\text{e}^- \rightarrow \text{H}_2$). However, most of the cathode materials have low reaction efficiency. To overcome this shortcoming, if the cathode surface were to be activated and the overpotential reduced, HER efficiency could greatly increase.

Recently, two-dimensional layered metal sulfides (MS) (i.e. MoS₂ [3,4], WS₂ [5], ZrS₃ [6], SnS [7,8], and SnS₂ [9,10]) were shown to have a unique graphene-like nanostructure. This excellent carrier mobility, due to the unique directionality in 2-D materials, and the narrow bandgap renders them as promising electrocatalysts for HER. Among the MS, SnS and related compounds appear to hold high potential for applications in HER [11,12]. The layer stacking and structural multiformity of SnS (ex: SnS,

SnS₂, Sn₂S₃, and Sn₃S₄) significantly enhance both the catalytic activity and electrical conductivity. SnS is a IV-VI group compound and the constituent elements are earth abundant and non-toxic, and so has attracted significant attention recently. Until now, the most common applications of SnS include Li-batteries [13], photovoltaic cells [14], photocatalysts [11], and electrocatalysts [12,15]. However, the low effective carrier density, Fermi pinning by the surface states of the electrode and electrolyte, carrier recombination at the boundaries by small grain sizes, and defects leading to carrier recombination at the junction have obstructed the HER efficiency of sulfides [16–18].

In response, efforts have been undertaken to enhance the surface conductivity/HER efficiency of MS via the addition of carbon-based materials [4,12], doping with various elements [7,19], surface modification [20,21], and surface plasma treatment techniques [22–27]. Efficiencies can also be enhanced by creating exposed active sites on the surface that can facilitate charge transfer. Among the several techniques proposed so far, atmospheric air plasma treatment (AAPT) is a simple, low-cost, stable processing method [23,24] to create active sites on the surface of the MS. Plasma treatments have been reported to enhance the activity and reduce defects of the MS reaction surface by using Cl [25], O₂ [22,27], amine (NH₃) [28], argon [29], and xenon difluoride (XeF₂) [30] as the carrier gases. However, these plasma approaches are toxic, and require a high vacuum system, regular maintenance, and significant capital expenditure.

In this paper, we attempt to enhance the surface activity of the SnS thin films by a safe, fast, and low-cost atmospheric air plasma treatment. In doing so, SnS thin films were treated at various plasma powers to investigate their properties. Herein, we describe a facile method to enhance SnS thin film electrocatalysts and demonstrate their excellent performance in HER.

2. Results

Figure 1a–c shows the X-ray diffraction (XRD) spectra of the SnS thin film without and with air plasma treatment at 150 W and 250 W, respectively. As seen, the pure SnS thin film (Figure 1a) shows only one (040) plane diffraction peak at $2\theta = 31.97^\circ$ (JCPDS 39-0354), which is because the SnS is stacked in the (040) plane along the b-axis [9]. The SnS thin films maintained an orthorhombic structure for all AAPT processes. In contrast, at 150 W power, the XRD result shows the (200) diffraction peak at $2\theta = 30.64^\circ$, which confirms the presence of elemental Sn (JCPDS 04-0673) [31]. A further increase of plasma power to 250 W eliminates the Sn (200) diffraction peak, but enables a new peak at $2\theta = 26.58^\circ$ to emerge, and is ascribed to SnO₂ JCPDS 71-0652 (110) [32].

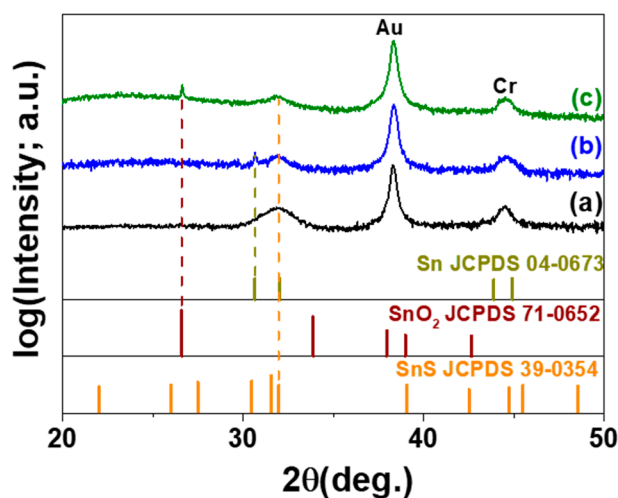


Figure 1. X-ray diffraction (XRD) patterns of the SnS thin film (a) without, and with (b) 150 W, and (c) 250 W atmospheric air plasma treatment.

Figure 2 shows the top view SEM images of the SnS thin films without and after AAPT at 150 W and 250 W power. Without AAPT, the SnS thin films demonstrate a relatively smooth surface without any visible cracks (Figure 2a). In comparison, the SnS thin films after AAPT feature a rougher surface (Figure 2b,c), which increases the area of exposed active sites that may contribute to enhanced HER efficiency on the working electrode. In the yellow insets of Figure 2b,c, it can be seen that the SnS nanocrystal is itself covered by fine nanocrystals; and, according to the XRD analysis, these may be Sn and SnO₂ nanocrystals.

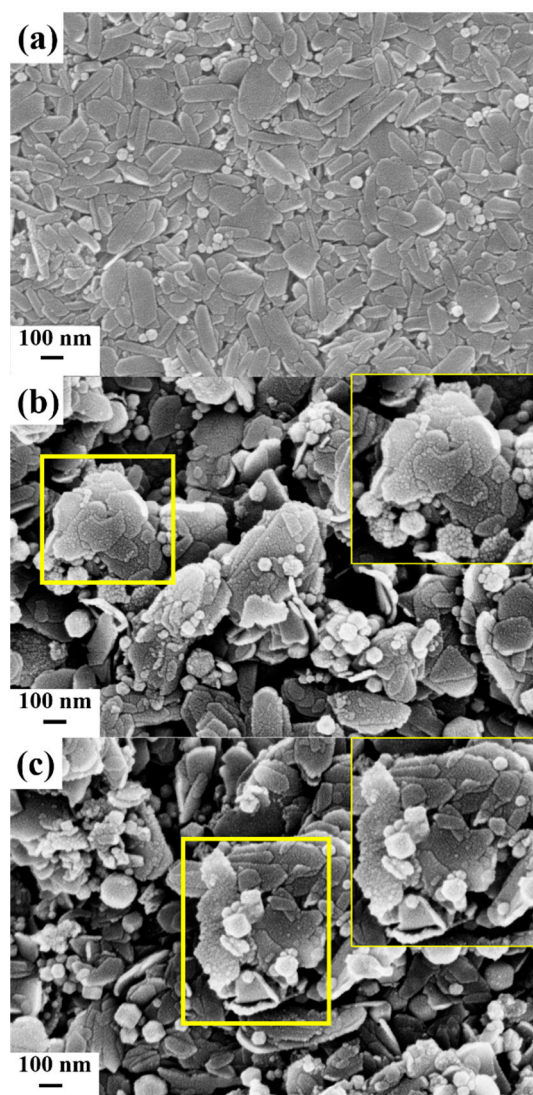


Figure 2. SEM images of the SnS thin films (a) without, and with (b) 150 W, and (c) 250 W atmospheric air plasma treatment.

The bright-field TEM image (Figure 3a) shows the existence of two different SnS-nanocrystal microstructures (hexagonal-shaped nanosheets and spherical nanoparticles) in the same matrix. In our previous study [33], we observed a metastable phase consisting of hexagonal nanosheets and spherical nanoparticles in transition from the cubic phase to the more stable orthorhombic phase, where the average spherical-nanoparticle size ranged between 20~40 nm. The high-resolution (HR) TEM image in Figure 3b shows two lattice spacing values of 2.35 Å and 2.88 Å (angle = 90°), which correspond to the (220) and (002) planes of the cubic-phase SnS, respectively. Moreover, the hexagonal SnS nanosheets are 200–400 nm long and 50–100 nm wide (Figure 3c), which agrees well with the SEM observations.

The SnS nanosheets comprise single crystals projected along the (010) direction, as shown by the selected area electron diffraction (SAED) pattern (Inset in Figure 3c). The HRTEM image in Figure 3d reveals a lattice spacing of 2.91 Å and 2.93 Å (angle = 90°), corresponding to the (101) and ($\bar{1}01$) planes of orthorhombic-phase SnS, respectively. The thickness of the SnS nanosheets is approximately 9 nm, as confirmed in the HRTEM images (Figure 3e,f). This finding agrees well with the SAXS (small-angle X-ray scattering shown in Figure S1) results using the generalized indirect Fourier transformation (GIFT), which revealed the formation of flat disks. The XRD data of the SnS thin films show a single peak corresponding to the (040) plane of orthorhombic SnS, which is attributed to the stacking of the SnS nanosheets on the substrate and growth along the (040) plane after spin coating [34,35].

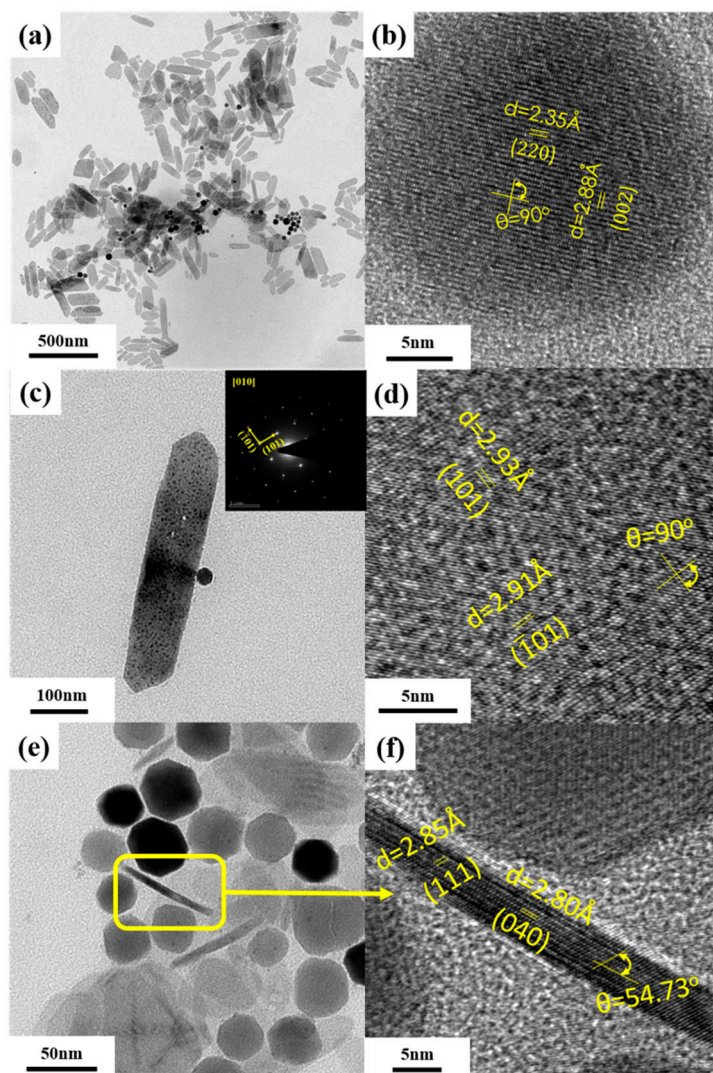


Figure 3. (a) TEM images of the SnS nanocrystals consisting of orthorhombic phase hexagonal SnS nanosheets and cubic phase SnS nanoparticles. (b) HRTEM image showing the crystal planes of cubic phase SnS. (c) TEM image showing the top view of the SnS nanosheet (Inset: selected area electron diffraction (SAED) patterns indexed to orthorhombic-SnS). (d) HRTEM top-view image of the SnS nanosheet showing crystal planes of orthorhombic SnS. (e) TEM image showing the cross-sectional view of the SnS nanosheet. (f) HRTEM image of SnS nanosheet cross-section showing stacked crystal planes of orthorhombic SnS.

Figure 4 shows the bright-field TEM images of the SnS nanocrystals after 150 W (Figure 4a,b) and 250 W (Figure 4c,d) of AAPT. The surfaces of the cubic SnS nanocrystals are themselves covered by

agglomerations of fine crystal precipitates (yellow area in Figure 4a) and the HRTEM image reveals lattice spacing values of 3.01 Å and 2.97 Å, both of which are in agreement with the (200) plane of metal Sn nanoparticles (2–3 nm) (Figure 4b). Figure 4c shows that plasma treatment at higher power (250 W) leads to further agglomeration of SnS nanocrystals with an approximate size of 500 nm, where the large structure shown in the image consists of numerous smaller SnS nanocrystals. The HRTEM image at the edge of the large agglomerated structure (the yellow area in Figure 4c) is displayed in Figure 4d, in which the lattice spacing values of 2.64 Å and 2.97 Å were obtained corresponding to the SnO₂ nanocrystal (101) plane. The SnO₂ nanocrystal size was approximately 5–7 nm, which is larger than a Sn nanocrystal (as shown in Figure 4b). Therefore, it may be concluded that the 150 W AAPT of SnS nanocrystal leads to a reduction in the SnS surface to Sn metal while the AAPT at 250 W causes the oxidation of the SnS surface to SnO₂.

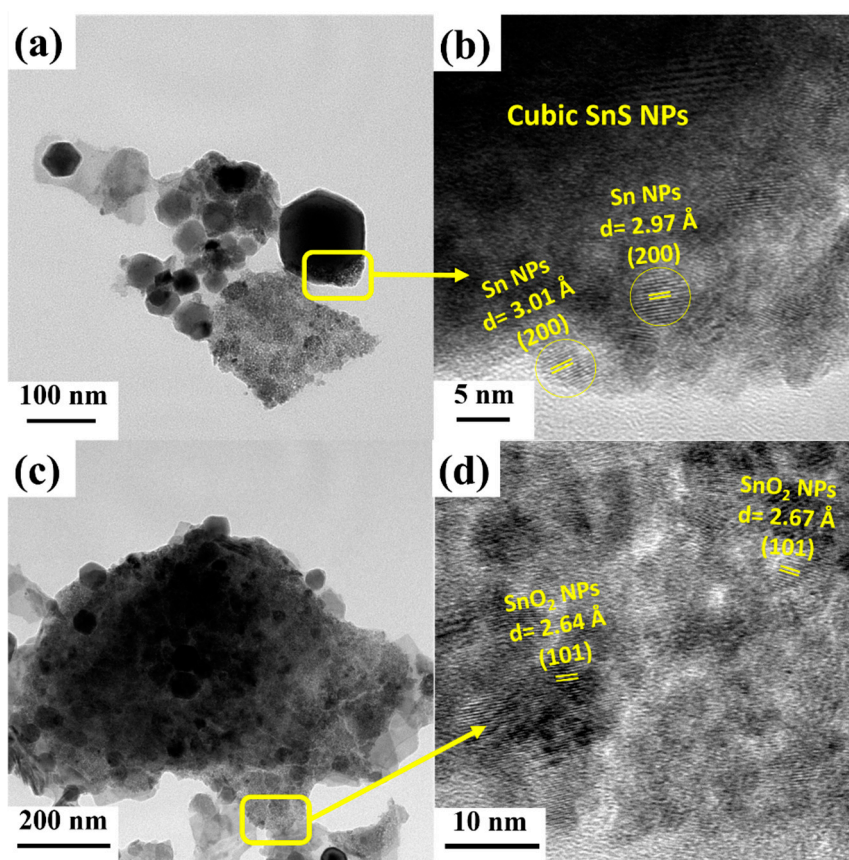


Figure 4. TEM bright field image and high-resolution image of SnS nanocrystals under (a,b) 150 W and (c,d) 250 W atmospheric air plasma treatment, respectively. The samples were prepared by stripping from different watt-treated SnS thin films.

Figure 5 shows the surface wettability image of the SnS thin films with and without AAPT. As seen, the SnS thin film has a contact angle of 131.68° (Figure 5a), which represents the surface hydrophobicity of SnS thin films. In comparison, after AAPT at 150 W and 250 W, the SnS thin film surface becomes hydrophilic (Figure 5b,c). The contact angle of the SnS thin film subjected to 150 W AAPT had a lower contact angle of 60.89°, indicating stronger hydrophilicity than with 250 W (80.07°). Usually, AAPT treatment increases the surface defects, thereby altering the surface from hydrophobic to hydrophilic, which provides a superior active surface for hydrogen-ion adsorption and desorption.

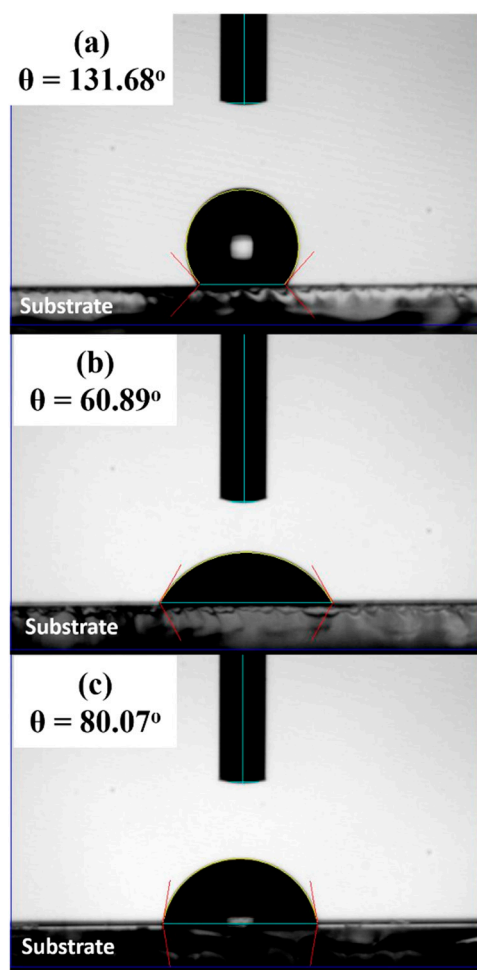


Figure 5. Water contact angle (WCA) images of SnS thin films surface (a) without, and with (b) 150 W and (c) 250 W atmospheric air plasma treatment (AAPT).

The surface atomic valence states and the chemical composition of the SnS thin films before and after AAPT treatment were analyzed using electron spectroscopy for chemical analysis (ESCA) (Figure 6). The Sn 3d peak and S 2p peak of the SnS appear at 485.5 eV and 161.7 eV, which respectively correspond to the Sn–S bonding and S–Sn bonding [9]. However, a trace amount of Sn=O bonding is still present in SnS. This may arise due to physical adsorption of oxygen on the SnS surface followed by formation of Sn=O bonds due to the presence of trace impurity Sn^{4+} ions. Therefore, in Figure 6c, the O1s peak intensity of C=O bonding (532.2 eV) intensity is relatively weak and can be ignored as compared to other AAPT treated samples. However, the Sn 3d, S 2p, and O1s peaks become asymmetric and their peak positions shift after AAPT. Specifically, the plasma treatment at 150 W leads to the oxidation of sulfide in SnS, and, therefore, in addition to the Sn–S bond at 485.5 eV, two other peaks are also observed at 486.7 eV (high-intensity Sn=O bond) [9] and at 484.8 eV (elemental Sn). The S 2p spectrum shows peaks at 161.7 eV and 160.7 eV, corresponding to Sn–S bonding [36]. The O1s peak at 531.6 eV 530.5 eV corresponds to Sn=O bonding [32,37]. However, the XRD result does not show any diffraction peak of SnO_2 ; rather, a peak corresponding to Sn is observed. Accordingly, at 150 W power, the SnO_2 is most probably in the amorphous phase (Figure 1b). The appearance of the elemental Sn peak is due to the incomplete oxidation of Sn after the oxidation of S, which evaporates as SO_2 and exposes the Sn metal over the surface. This occurrence is beneficial for HER performance by enhancing the active edge sites. In contrast, an elemental Sn peak is not observed at 250 W due to the complete conversion of the entire Sn surface to SnO_2 .

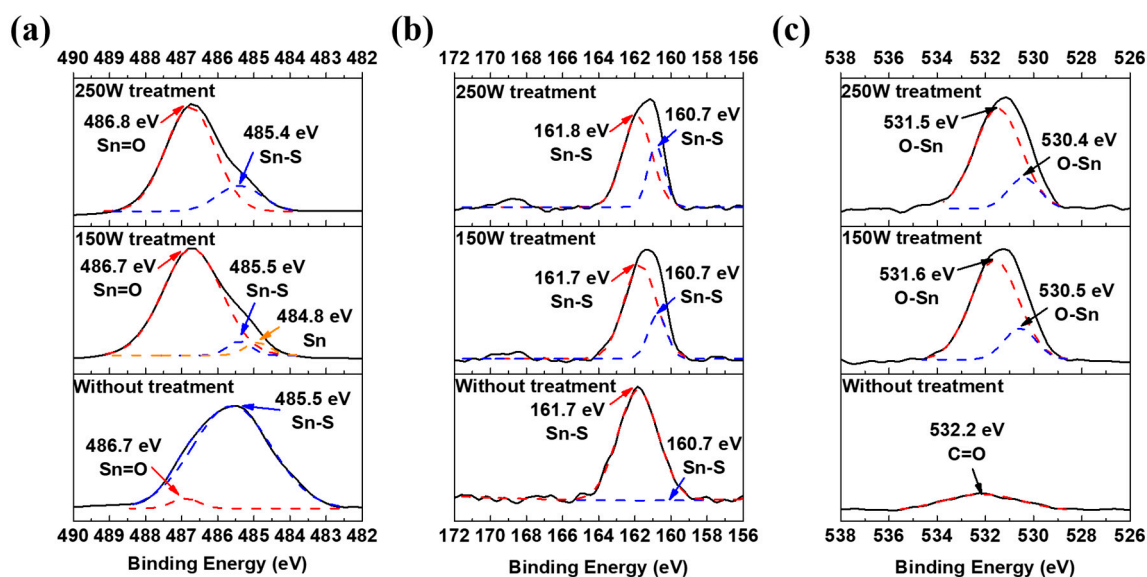


Figure 6. Electron spectroscopy for chemical analysis (ESCA) core level spectra analysis of the (a) $\text{Sn}3d_{5/2}$ peak, (b) $\text{S}2p_{1/2}$ peak and (c) $\text{O}1s$ peak for the untreated SnS thin films and with 150 W and 250 W AAPT.

Figure 7 shows the valence band maximum (VBM) fitting plots and ESCA elemental composition ratio of SnS before and after AAPT. It should be noted that the initial binding energies of Sn 3d, S 2p, and the VBM [36] may vary by sample due to the n/p-type nature of SnS, which might originate from stoichiometry variations and/or structural defects [27], such as surface steps and dislocations. To better understand the stoichiometry evolution of SnS after AAPT treatment (150–250 W power) and without treatment, all samples with similar chemical states and stoichiometry in Table 1 were chosen. After the AAPT with various working power densities, the VBM in Figure 7a shifted in binding energy value. Such shifts represent the Fermi-level realignment-induced band-bending [38], which can be evaluated by the VBM obtained from the valence band region (see Figure 7a and Table 1).

In Figure 7a, the binding energy at 0 eV represents the Fermi level (E_F) and the VBM of the SnS thin films before AAPT relative to the Fermi level is 1.31 eV which is very close to the intrinsic band gap of bulk SnS [39]. The composition (at%) ratio of S/Sn of SnS before AAPT was 0.78 (as shown in Figure 7b and Table 1) while the VBM of the as-prepared SnS was 1.31 eV.

After 150 W AAPT, the VBM shifted downward to 0 eV (Figure 7a), and the composition ratio of S/Sn decreased to 0.20 (Figure 7b). During AAPT treatment, the oxygen ions in the plasma reacted with the S atoms over the surface of SnS, thereby evaporating the S atoms as SO_2 and generating a number of S-vacancies. Accordingly, the resulting S-vacancies shifted the surface states to the conduction band edge and introduced a strong p-type pinning effect on the SnS.

When the AAPT power was increased to 250 W, the VBM shifted downward to 0.76 eV (Figure 7a) and the ratio of S/Sn increased slightly to 0.31, and atomic percent of O increased greatly to 49.0% (Figure 7b). Compared to the XRD (Figure 1) results, SnO_2 existed under the 250 W AAPT state; therefore, the SnS surface state due to the O introduced a strong n-type pinning effect on the SnS [27].

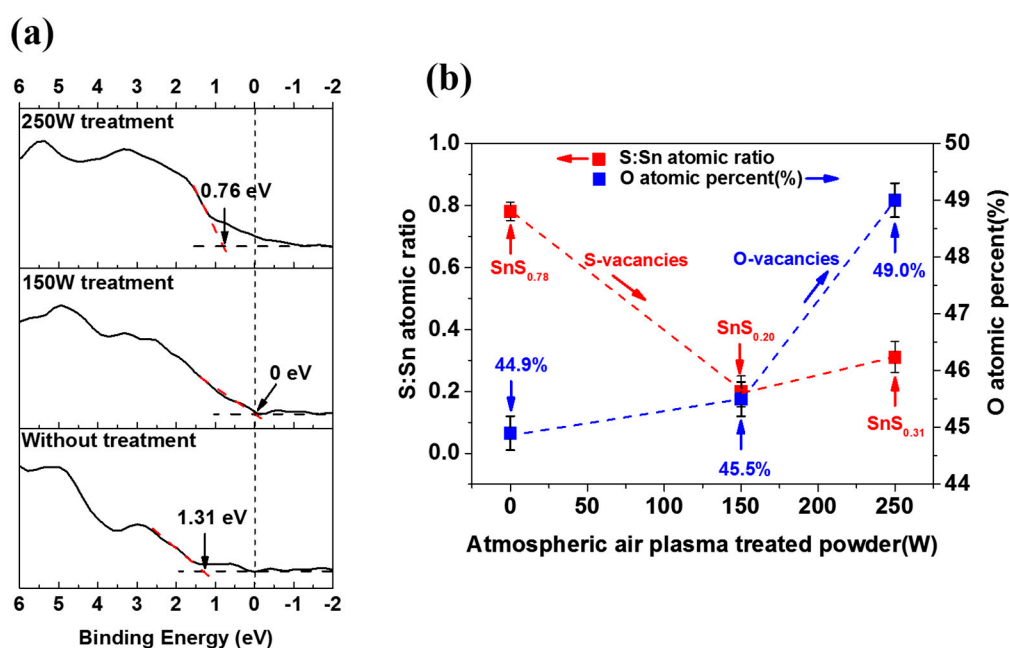


Figure 7. (a) Valence band maxima (VBM) fitting; and, (b) O atomic percentage and S/Sn atomic ratio plot for the SnS thin films before and after AAPT.

Table 1. Summary of the measured valence band maxima (VBM) fitting, atomic percentages (Sn, S, and O), and atomic ratio (S/Sn) from the SnS thin films before and after atmospheric air plasma treatment (AAPT).

Sample Name	VBM	Atom % (Sn)	Atom % (S)	Atom % (O)	S/Sn Ratio
Without AAPT	1.31	30.8	24.3	44.9	0.78
150 W AAPT	0	45.4	9.1	45.5	0.20
250 W AAPT	0.76	38.9	12.1	49.0	0.31

Figure 8 shows the electrocatalytic performance of SnS before and after AAPT at different powers (150 W, 250 W). The as-prepared SnS thin films without AAPT displayed a weak current density of -0.224 mA/cm^2 when the applied potential was -0.325 V (Figure 8a). In comparison, the SnS thin films after 150 W AAPT showed superior electrocatalytic performance with a current density of -10 mA/cm^2 at the same applied potential, which was significantly higher than with AAPT at 250 W. After the 250 W AAPT, the SnS thin films underwent a deterioration of electrocatalytic current density (onset: -150 mV ; -0.394 mA/cm^2 at -325 mV).

The Tafel slopes (Figure 8b) were determined by fitting the linear portions of the Tafel plots to the Tafel equation ($\eta = b \log j + a$), where j is the current density, a is the empirical coefficient, and b is the Tafel slope. The overall HER mechanism in acidic media is described through three principle steps, namely the Volmer reaction ($\text{H}^+ + \text{M} + e^- \rightarrow \text{M} - \text{H}^*$, Tafel slope $\sim 120 \text{ mV/dec}$), the Heyrovsky reaction ($\text{M} - \text{H}^* + \text{M} + e^- \rightarrow \text{M} + \text{H}_2$, Tafel slope $\sim 40 \text{ mV/dec}$), and the Tafel reaction ($2\text{M} - \text{H}^* \rightarrow 2\text{M} + \text{H}_2$, Tafel slope $\sim 30 \text{ mV/dec}$) [1,40], where M is the electrode surface and H^* is an adsorbed hydrogen atom. Experimentally, the two main pathways through which the HER reaction proceeds are either the Volmer–Heyrovsky reaction or the Volmer–Tafel reaction.

Table 2 describes the detail electrochemical parameters of SnS thin films after different plasma process treatment. The Tafel plots show slopes of 174 mV/dec for the as-prepared SnS; meanwhile, a significantly lower value of 60 mV/dec is observed for the SnS after 150 W AAPT (Figure 8b) but a higher Tafel slope value of 210 mV/dec after AAPT at 250 W. The low Tafel slope (60 mV/dec) for the SnS after 150 W AAPT indicates that the HER most probably occurs via the Volmer–Heyrovsky

mechanism, where the electron reduction of protons provides a hydrogen atom bound to an active site (Volmer reaction) and also leads to the electrochemical desorption of hydrogen (Heyrovsky reaction).

The stability test of SnS thin film after 150 W AAPT at -325 mV vs. RHE for 5400 s is shown in Figure S3. The plasma treated SnS thin films displayed current densities of -9.63 mA/cm², -9.22 mA/cm² and -9.53 mA/cm² at 1800 s, 3600 s and 5400 s, respectively. Consequently, the SnS thin films after 150 W AAPT demonstrate a good stable HER current density and the value is much higher than our previous report using SnS thin films without AAPT [9,33].

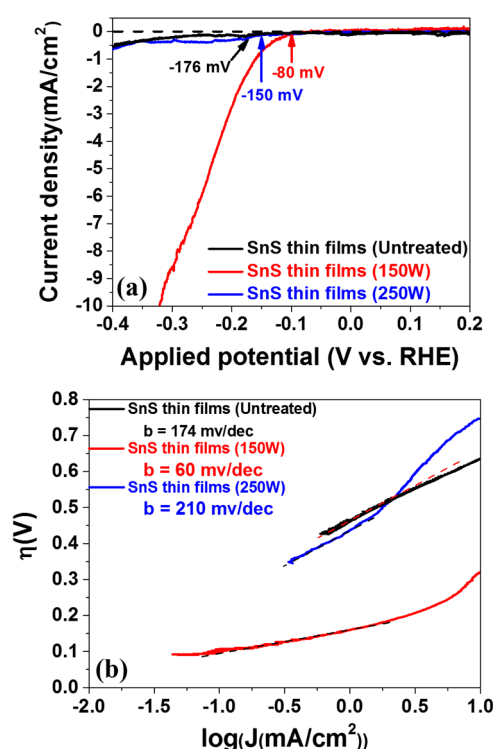


Figure 8. (a) Linear sweep voltammetry curves at the scan rate of 5 mV/s for the SnS thin films without treatment, and with 150 W and 250 W AAPT. (b) The corresponding Tafel plots for the SnS thin films without treatment, and with 150 W and 250 W AAPT.

Table 2. Comparison of the main electrochemical parameters in the hydrogen evolution reaction (HER) for the SnS thin films under different plasma process treatments.

Sample Name	Onset (mV)	Current Density (-325 mV)	Tafel Slope
Without AAPT	-176 mV	-0.224 mA/cm ²	174 mV/dec
150 W AAPT	-80 mV	-10 mA/cm ²	60 mV/dec
250 W AAPT	-150 mV	-0.394 mA/cm ²	210 mV/dec

Optical measurements of SnS thin films after 150 W AAPT show absorption onsets at about 800 nm (Support information Figure S2). The relationship between the absorption coefficient (α) and the energy of the incident photon for semiconductors can be expressed as $(\alpha h\nu)^n = B(h\nu - E_g)$, where B is a constant and n is a number that depends on the electronic transition of the semiconductor. The dependence of α^2 (for $n = 2$) on the photon energy ($h\nu$) for the direct band gap semiconductor is illustrated graphically in Figure 6f. The direct band gap (E_g) for the SnS thin films after 150 W treatment can be estimated by the intercepts of the plot after extrapolation and has a value of about 1.55 eV (as shown in Figure S2).

Schematic energy band diagrams of the SnS thin films without and with AAPT are shown in Figure 9. Initially, the valance band (E_{VBM}) and the SnS band (E_g) were investigated by VBM as shown in Figure 7a and UV-Vis as shown in Figure S2, respectively. The positions of different energy levels in

the as-prepared SnS (Figure 9a) were similar to our previous report (SnS at equilibrium) [9], which found that the moderate catalytic properties were due to the thicker space charge layer and excess barrier [9]. In this study, the SnS thin films after 150 W AAPT had more metal active edges (due to S-vacancy) and a more hydrophilic surface, the combined effect of which facilitated an easier pathway for electron transport and hydrogen adsorption and desorption. The S-vacancy introduced a p-type pinning effect which resulted in an upward shift of the conduction band position which was higher than the hydrogen reduction position (Figure 9b). Formation of the metal active edge, hydrophilic surface and the p-type pinning demonstrate a Volmer–Heyrovsky-type reaction with a Tafel slope of 60 mV/dec.

In contrast, for the 250 W AAPT SnS samples, HER proceeded through the Volmer reaction, as suggested by its large Tafel slope of 210 mV/dec. The relatively hydrophobic nature and n-type pinning effect led to less active properties of the SnS thin films, which limited the rate of HER kinetics (Figure 9c).

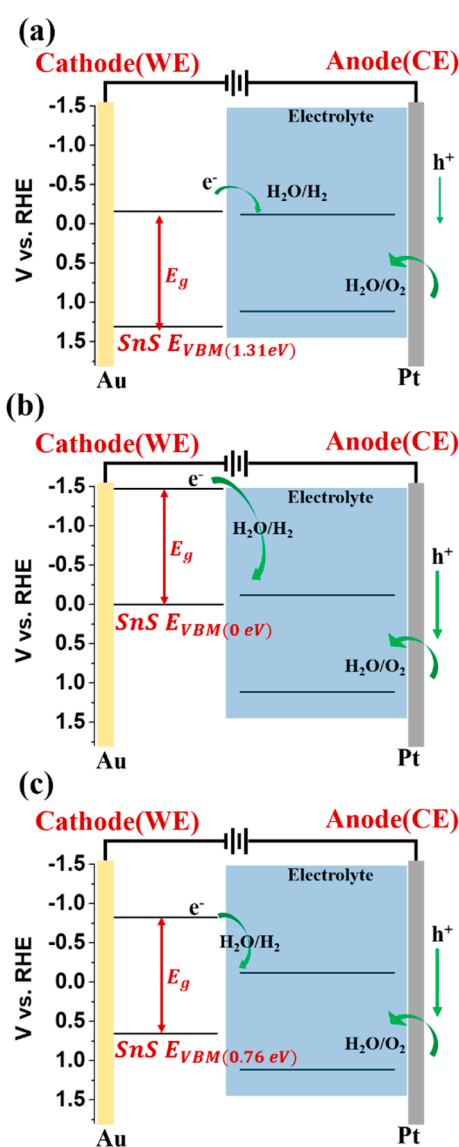


Figure 9. Schematic energy band diagrams of SnS (a) without, and with (b) 150 W and (c) 250 W AAPT.

Table S1 (Supplementary information) summarizes the current density, applied overpotential and Tafel slopes from previously published reports. Our SnS thin film electrocatalysts after 150 W AAPT feature a much higher current density and lower Tafel slope as compared to previously reported

TMD electrocatalysts [12,41–46]. Although, SnS exhibits excellent catalytic properties for HER, it still requires a high operating overpotential. This drawback must be reduced to ensure it can be a viable alternative catalyst to the Pt-group metals, which operate at negligible overpotentials. As shown in Table S1, a commonly-used protocol to reduce the high operating overpotential is to combine the working electrode with a conductive material [12,41–44,47,48]. In future studies, we will conduct such experiments to reduce the operating overpotential and enhance the catalytic efficiency by incorporating conductive nanomaterials.

3. Materials and Methods

3.1. Synthesis of Mixed Phase SnS Nanocrystals

The SnS nanocrystal powder was synthesized under optimized reaction conditions with the hot injection method [9,10,33,49]. Following a typical synthesis protocol, 1.35 g of SnO (Tin (II) Oxide, SHOWA, 99%, Osaka, Japan) was mixed with 13.5 mL OA (Oleic Acid, Sigma Aldrich, 66%–88%, St. Louis, MO, US) in a three-neck flask and heated to 120 °C under argon gas flow for 15 min. The mixture was then heated further to 280 °C to form the tin precursor, Sn(OA)_x, after which it was cooled to 190 °C naturally. At this point, the hot sulfur precursor, S-OLA (0.45 mmol of sulfur powder, Sigma Aldrich, 98% (St. Louis, MO, US), 9 mL of Oleylamine, ACROS, 90%, Geel, Belgium), was quickly injected into the tin precursor with glass syringes and the final temperature maintained at 190 °C for 30 min and cooled immediately to room temperature in ice bath condition. All chemicals were used without further purification. The resulting SnS nanoparticle solution was then added to ethanol and acetone for centrifugation for several times [9,49]. Finally, the SnS nanocrystal powder was dried under vacuum or re-dispersed in hexane for further characterization. The synthesized SnS nanocrystals (2 mg) were then dispersed in toluene (2 mL) and spin coated on the glass/Cr/Au (50 nm/70 nm) substrate followed by vacuum drying for 5 min at 85 °C.

3.2. Atmospheric Air Plasma Treatment

The SnS thin films were treated at atmospheric-pressure, and with air as the plasma carrier gas. A similar experimental arrangement of atmospheric air plasma treatment (AAPT) is described in detail in [24]. The power consumption of the plasmas were 0 W, 150 W, and 250 W for 20 s. A schematic of the setup used for AAPT on the SnS thin films is shown in Figure 10.

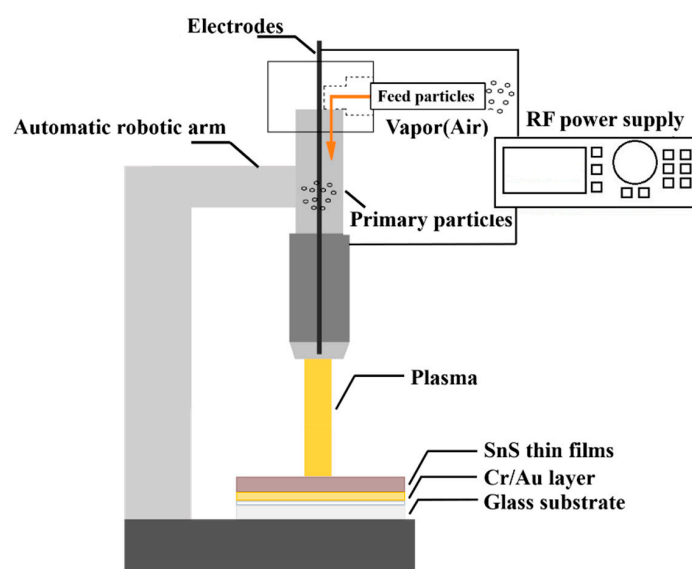


Figure 10. Schematic diagram of the atmospheric air plasma treatment for the SnS thin films used in this work.

3.3. Material Characterization

X-ray diffraction (XRD) was performed on a Bruker D2 diffractometer (D2 Phaser, BRUKER, Karlsruhe, Germany) with Cu K α radiation ($\lambda = 1.54178 \text{ \AA}$) at a scan rate of $0.025^\circ \text{ s}^{-1}$ from $2\theta = 20\text{--}50^\circ$ for structural analysis. Microstructure analysis was given by the field emission gun transmission electron microscope (Tecnai G2 F20 FEG-TEM, Amsterdam, Netherlands) at an acceleration voltage of 200 kV. Thin films surface morphology was investigated by using the field emission scanning electron microscopy (UHRFE-SEM, Zeiss, Auriga, Oberkochen, Germany). Electron spectroscopy for chemical analysis (ESCA, PHI-5000, Waltham, MA, USA) measurements were performed with an exciting source of Mg K $\alpha = 1253.6 \text{ eV}$. The binding energies obtained in the ESCA spectral analysis were corrected by referencing C 1 s to 284.5 eV. UV–Vis absorption spectra were obtained using a spectrophotometer equipped with an integrating sphere (JASCO V-650, Tokyo, Japan).

3.4. SnS Electrochemical Measurements

A three electrode cell configuration was utilized with the SnS (0, 150 W and 250 W AAPT) as the working electrode (WE), platinum as the counter electrode (CE), and Ag/AgCl (3.0 mol/kg KCl) as the reference electrode (RE) in a 0.5 M H₂SO₄ electrolyte (pH = 0). A radiometer analytical potentiostat (Volta lab PGZ301) was used to perform electrochemical measurements, and the obtained polarization data were calibrated with respect to the reversible hydrogen electrode (RHE) by $E_{RHE} = 0 - (E_{RE} + 0.059 \times \text{pH})$. Linear sweep voltammetry was employed to produce polarization plots with a fixed scan rate of 5 mV/s under the applied potentials from -0.5 to 0.2 V vs. RHE.

4. Conclusions

We reported the use of a simple, low cost, stable, 20 s atmospheric air plasma treatment (AAPT) for SnS thin films for enhanced HER performance. SnS thin films maintain the crystallographic structure in the bulk after AAPT, but, the surface changes significantly by different AAPT power with the formation of S-vacancies, formation of active Sn edge sites at 150 W, and surface oxidation at 250 W. AAPT of SnS thin films at an intermediate power (150 W) can greatly enhance the electrocatalytic performance due to the presence of the Sn active edge sites on the surface of the SnS thin films, the introduction of p-type pinning induced by the S-vacancy, and the formation of the hydrophilic surface. The detailed HER mechanism is explained by a suitable band diagram where the conduction and valence band positions are obtained from UV–Vis and ESCA–VBM measurements. Therefore, SnS thin films show excellent catalytic properties after AAPT without any secondary materials or complicated synthesis processes. Given our encouraging findings, we anticipate future advances in tin sulfide materials as a promising alternative to precious metal electrocatalysts for sustainable hydrogen generation.

Supplementary Materials: The following are available online at <http://www.mdpi.com/2073-4344/8/10/462/s1>, Figure S1: SAXS radiation of SnS nanocrystals: (a) real data (b) pair distance distribution function (PDDF) data, Figure S2: (a) UV–Vis absorption spectra as a function of incident photon wavelength for SnS thin films after 150 W AAPT treatment. (b) Extrapolation of direct bandgap value of SnS thin films after 150 W AAPT treatment, Figure S3: (a) SnS thin film at -325 mV vs. RHE for 5400 s stabilized test, Table S1: Literature properties of HER catalysts (as mentioned in the main text).

Author Contributions: Conceptualization, P.-C.H., S.B., J.L.H. and S.-C.W.; Methodology, P.-C.H., P.-Y.L., S.-C.W. and M.O.S.; Investigation, P.C.H. and P.-Y.L.; Resources, J.-L.H. and S.-C.W.; Data Curation, P.-C.H.; Writing–Original Draft Preparation, P.-C.H. and S.B.; Writing–Review & Editing, P.-C.H., S.B., S.-C.W. and M.O.S.; Supervision, J.-L.H. and S.-C.W.; Project Administration, J.-L.H. and S.-C.W.

Funding: This research was funded by the Ministry of Science and Technology of the ROC grant number MOST 107-2221-E-218-003- and MOST 107-3017-F-006-003-.

Acknowledgments: Authors would like to thank the technical support from Cheng Yen Chen (JUMBO Applied Engineering Co., Ltd.).

Conflicts of Interest: The authors declare no conflict of interest.

References

1. Wang, F.M.; Shifa, T.A.; Zhan, X.Y.; Huang, Y.; Liu, K.L.; Cheng, Z.Z.; Jiang, C.; He, J. Recent advances in transition-metal dichalcogenide based nanomaterials for water splitting. *Nanoscale* **2015**, *7*, 19764–19788. [[CrossRef](#)] [[PubMed](#)]
2. Gao, M.R.; Xu, Y.F.; Jiang, J.; Yu, S.H. Nanostructured metal chalcogenides: Synthesis, modification, and applications in energy conversion and storage devices. *Chem. Soc. Rev.* **2013**, *42*, 2986–3017. [[CrossRef](#)] [[PubMed](#)]
3. Wu, C.L.; Huang, P.C.; Brahma, S.; Huang, J.L.; Wang, S.C. MoS₂-MoO₂ composite electrocatalysts by hot-injection method for hydrogen evolution reaction. *Ceram. Int.* **2017**, *43*, S621–S627. [[CrossRef](#)]
4. Li, P.; Yang, Z.; Shen, J.; Nie, H.; Cai, Q.; Li, L.; Ge, M.; Gu, C.; Chen, X.A.; Yang, K. Subnanometer Molybdenum Sulfide on Carbon Nanotubes as a Highly Active and Stable Electrocatalyst for Hydrogen Evolution Reaction. *ACS Appl. Mater. Interfaces* **2016**, *8*, 3543–3550. [[CrossRef](#)] [[PubMed](#)]
5. Sang, Y.H.; Zhao, Z.H.; Zhao, M.W.; Hao, P.; Leng, Y.H.; Liu, H. From UV to Near-Infrared, WS₂ Nanosheet: A Novel Photocatalyst for Full Solar Light Spectrum Photodegradation. *Adv. Mater.* **2015**, *27*, 363–369. [[CrossRef](#)] [[PubMed](#)]
6. Xie, J.F.; Wang, R.X.; Bao, J.; Zhang, X.D.; Zhang, H.; Li, S.; Xie, Y. Zirconium trisulfide ultrathin nanosheets as efficient catalysts for water oxidation in both alkaline and neutral solutions. *Inorg. Chem. Front.* **2014**, *1*, 751–756. [[CrossRef](#)]
7. Kafashan, H.; Azizieh, M.; Balak, Z. Electrochemical synthesis of nanostructured Se-doped SnS: Effect of Se-dopant on surface characterizations. *Appl. Surf. Sci.* **2017**, *410*, 186–195. [[CrossRef](#)]
8. Kois, J.; Bereznev, S.; Maricheva, J.; Revathi, N. Electrochemical and photoelectrochemical characterization of SnS photoabsorber films. *Mater. Sci. Semicond. Process.* **2017**, *58*, 76–81. [[CrossRef](#)]
9. Huang, P.C.; Shen, Y.M.; Brahma, S.; Shaikh, M.O.; Huang, J.L.; Wang, S.C. SnS_x (x = 1, 2) Nanocrystals as Effective Catalysts for Photoelectrochemical Water Splitting. *Catalysts* **2017**, *7*, 252. [[CrossRef](#)]
10. Huang, P.C.; Wang, H.I.; Brahma, S.; Wang, S.C.; Huang, J.L. Synthesis and characteristics of layered SnS₂ nanostructures via hot injection method. *J. Cryst. Growth* **2017**, *468*, 162–168. [[CrossRef](#)]
11. Patel, M.; Chavda, A.; Mukhopadhyay, I.; Kim, J.; Ray, A. Nanostructured SnS with inherent anisotropic optical properties for high photoactivity. *Nanoscale* **2016**, *8*, 2293–2303. [[CrossRef](#)] [[PubMed](#)]
12. Shinde, S.S.; Sami, A.; Kim, D.H.; Lee, J.H. Nanostructured SnS-N-doped graphene as an advanced electrocatalyst for the hydrogen evolution reaction. *Chem. Commun.* **2015**, *51*, 15716–15719. [[CrossRef](#)] [[PubMed](#)]
13. Zhao, B.; Wang, Z.X.; Chen, F.; Yang, Y.Q.; Gao, Y.; Chen, L.; Jiao, Z.; Cheng, L.L.; Jiang, Y. Three-Dimensional Interconnected Spherical Graphene Framework/SnS Nanocomposite for Anode Material with Superior Lithium Storage Performance: Complete Reversibility of Li₂S. *ACS Appl. Mater. Interfaces* **2017**, *9*, 1407–1415. [[CrossRef](#)] [[PubMed](#)]
14. Hortikar, S.S.; Kadam, V.S.; Rathi, A.B.; Jagtap, C.V.; Pathan, H.M.; Mulla, I.S.; Adhyapak, P.V. Synthesis and deposition of nanostructured SnS for semiconductor-sensitized solar cell. *J. Solid State Electrochem.* **2017**, *21*, 2707–2712. [[CrossRef](#)]
15. Chia, X.Y.; Lazar, P.; Sofer, Z.; Luxa, J.; Pumera, M. Layered SnS versus SnS₂: Valence and Structural implications on Electrochemistry and Clean Energy Electrocatalysis. *J. Phys. Chem. C* **2016**, *120*, 24098–24111. [[CrossRef](#)]
16. Ennaoui, A.; Fiechter, S.; Jaegermann, W.; Tributsch, H. Photoelectrochemistry of Highly Quantum Efficient Single-Crystalline N-Fes₂ (Pyrite). *J. Electrochem. Soc.* **1986**, *133*, 97–106. [[CrossRef](#)]
17. Todorov, T.K.; Tang, J.; Bag, S.; Gunawan, O.; Gokmen, T.; Zhu, Y.; Mitzi, D.B. Beyond 11% Efficiency: Characteristics of State-of-the-Art Cu₂ZnSn(S,Se)₄ Solar Cells. *Adv. Energy Mater.* **2013**, *3*, 34–38. [[CrossRef](#)]
18. Wang, W.; Winkler, M.T.; Gunawan, O.; Gokmen, T.; Todorov, T.K.; Zhu, Y.; Mitzi, D.B. Device Characteristics of CZTSSe Thin-Film Solar Cells with 12.6% Efficiency. *Adv. Energy Mater.* **2014**, *4*, 1301465. [[CrossRef](#)]
19. Chaki, S.H.; Chaudhary, M.D.; Deshpande, M.P. Effect of Indium and Antimony Doping on SnS Photoelectrochemical Solar Cells. *Chin. Phys. Lett.* **2014**, *31*, 10. [[CrossRef](#)]
20. Sun, Y.F.; Gao, S.; Lei, F.C.; Xie, Y. Atomically-thin two-dimensional sheets for understanding active sites in catalysis. *Chem. Soc. Rev.* **2015**, *44*, 623–636. [[CrossRef](#)] [[PubMed](#)]

21. Yin, Z.Y.; Chen, B.; Bosman, M.; Cao, X.H.; Chen, J.Z.; Zheng, B.; Zhang, H. Au Nanoparticle-Modified MoS₂ Nanosheet-Based Photoelectrochemical Cells for Water Splitting. *Small* **2014**, *10*, 3537–3543. [[CrossRef](#)] [[PubMed](#)]
22. Gomez, A.; Martinez, H.; Calixto-Rodriguez, M.; Avellaneda, D.; Reyes, P.G.; Flores, O. Modification of optical and electrical properties of chemical bath deposited SnS using O-2 plasma treatments. *Appl. Surf. Sci.* **2013**, *275*, 273–277. [[CrossRef](#)]
23. Chu, X.M.S.; Li, D.O.; Green, A.A.; Wang, Q.H. Formation of MoO₃ and WO₃ nanoscrolls from MoS₂ and WS₂ with atmospheric air plasma. *J. Mater. Chem. C* **2017**, *5*, 11301–11309. [[CrossRef](#)]
24. Lisco, F.; Shaw, A.; Wright, A.; Walls, J.M.; Iza, F. Atmospheric-pressure plasma surface activation for solution processed photovoltaic devices. *Sol. Energy* **2017**, *146*, 287–297. [[CrossRef](#)]
25. Lin, T.; Kang, B.; Jeon, M.; Huffman, C.; Jeon, J.; Lee, S.; Han, W.; Lee, J.; Lee, S.; Yeom, G.; et al. Controlled Layer-by-Layer Etching of MoS₂. *ACS Appl. Mater. Interfaces* **2015**, *7*, 15892–15897. [[CrossRef](#)] [[PubMed](#)]
26. Shin, Y.J.; Wang, Y.Y.; Huang, H.; Kalon, G.; Wee, A.T.S.; Shen, Z.X.; Bhatia, C.S.; Yang, H. Surface-Energy Engineering of Graphene. *Langmuir* **2010**, *26*, 3798–3802. [[CrossRef](#)] [[PubMed](#)]
27. Zhu, H.; Qin, X.Y.; Cheng, L.X.; Azcatl, A.; Kim, J.; Wallace, R.M. Remote Plasma Oxidation and Atomic Layer Etching of MoS₂. *ACS Appl. Mater. Interfaces* **2016**, *8*, 19119–19126. [[CrossRef](#)] [[PubMed](#)]
28. Dou, S.; Tao, L.; Huo, J.; Wang, S.Y.; Dai, L.M. Etched and doped Co₉S₈/graphene hybrid for oxygen electrocatalysis. *Energy Environ. Sci.* **2016**, *9*, 1320–1326. [[CrossRef](#)]
29. Li, H.; Tsai, C.; Koh, A.L.; Cai, L.L.; Contryman, A.W.; Fragapane, A.H.; Zhao, J.H.; Han, H.S.; Manoharan, H.C.; Abild-Pedersen, F.; et al. Activating and optimizing MoS₂ basal planes for hydrogen evolution through the formation of strained sulphur vacancies. *Nat. Mater.* **2016**, *15*, 48. [[CrossRef](#)] [[PubMed](#)]
30. Huang, Y.; Wu, J.; Xu, X.F.; Ho, Y.D.; Ni, G.X.; Zou, Q.; Koon, G.K.W.; Zhao, W.J.; Castro Neto, A.H.; Eda, G.; et al. An innovative way of etching MoS₂: Characterization and mechanistic investigation. *Nano Res.* **2013**, *6*, 200–207. [[CrossRef](#)]
31. Zhang, N.; Zhao, Q.; Han, X.P.; Yang, J.G.; Chen, J. Pitaya-like Sn@C nanocomposites as high-rate and long-life anode for lithium-ion batteries. *Nanoscale* **2014**, *6*, 2827–2832. [[CrossRef](#)] [[PubMed](#)]
32. Wang, X.L.; Wang, X.; Di, Q.Y.; Zhao, H.L.; Liang, B.; Yang, J.K. Mutual Effects of Fluorine Dopant and Oxygen Vacancies on Structural and Luminescence Characteristics of F Doped SnO₂ Nanoparticles. *Materials* **2017**, *10*, 1398. [[CrossRef](#)] [[PubMed](#)]
33. Huang, P.C.; Huang, J.L.; Wang, S.C.; Shaikh, M.O.; Lin, C.Y. Photoelectrochemical properties of orthorhombic and metastable phase SnS nanocrystals synthesized by a facile colloidal method. *Thin Solid Films* **2015**, *596*, 135–139. [[CrossRef](#)]
34. Herron, S.M.; Tanskanen, J.T.; Roelofs, K.E.; Bent, S.F. Highly Textured Tin(II) Sulfide Thin Films Formed from Sheetlike Nanocrystal Inks. *Chem. Mater.* **2014**, *26*, 7106–7113. [[CrossRef](#)]
35. Reddy, N.K. Growth-Temperature Dependent Physical Properties of SnS Nanocrystalline Thin Films. *ECS J. Solid State Sci. Technol.* **2013**, *2*, 259–263. [[CrossRef](#)]
36. Whittles, T.J.; Burton, L.A.; Skelton, J.M.; Walsh, A.; Veal, T.D.; Dhanak, V.R. Band Alignments, Valence Bands, and Core Levels in the Tin Sulfides SnS, SnS₂, and Sn₂S₃: Experiment and Theory. *Chem. Mater.* **2016**, *28*, 3718–3726. [[CrossRef](#)]
37. Zeng, Y.; Luo, J.Z.; Wang, Y.Z.; Qiao, L.; Zou, B.; Zheng, W.T. Controllable formation of multi-layered SnO₂@Fe₂O₃ sandwich cubes as a high-performance anode for Li-ion batteries. *Nanoscale* **2017**, *9*, 17576–17584. [[CrossRef](#)] [[PubMed](#)]
38. Burton, L.A.; Whittles, T.J.; Hesp, D.; Linhart, W.M.; Skelton, J.M.; Hou, B.; Webster, R.F.; O'Dowd, G.; Reece, C.; Cherns, D.; et al. Electronic and optical properties of single crystal SnS₂: An earth-abundant disulfide photocatalyst. *J. Mater. Chem. A* **2016**, *4*, 1312–1318. [[CrossRef](#)]
39. Liang, B.Y.J.; Shen, Y.M.; Wang, S.C.; Huang, J.L. The influence of reaction temperatures and volume of oleic acid to synthesis SnS nanocrystals by using thermal decomposition method. *Thin Solid Films* **2013**, *549*, 159–164. [[CrossRef](#)]
40. Conway, B.E.; Tilak, B.V. Interfacial processes involving electrocatalytic evolution and oxidation of H₂, and the role of chemisorbed H. *Electrochim. Acta* **2002**, *47*, 3571–3594. [[CrossRef](#)]
41. Chen, W.F.; Wang, C.H.; Sasaki, K.; Marinkovic, N.; Xu, W.; Muckerman, J.T.; Zhu, Y.; Adzic, R.R. Highly active and durable nanostructured molybdenum carbide electrocatalysts for hydrogen production. *Energy Environ. Sci.* **2013**, *6*, 943–951. [[CrossRef](#)]

42. Ma, L.; Zhou, X.P.; Xu, X.Y.; Xu, L.M.; Zhang, L.L.; Chen, W.X. One-step hydrothermal synthesis of few-layered and edge-abundant MoS₂/C nanocomposites with enhanced electrocatalytic performance for hydrogen evolution reaction. *Adv. Powder Technol.* **2015**, *26*, 1273–1280. [[CrossRef](#)]
43. Nikam, R.D.; Lu, A.Y.; Sonawane, P.A.; Kumar, U.R.; Yadav, K.; Li, L.J.; Chen, Y.T. Three-Dimensional Heterostructures of MoS₂ Nanosheets on Conducting MoO₂ as an Efficient Electrocatalyst To Enhance Hydrogen Evolution Reaction. *ACS Appl. Mater. Interfaces* **2015**, *7*, 23328–23335. [[CrossRef](#)] [[PubMed](#)]
44. Shifa, T.A.; Wang, F.M.; Cheng, Z.Z.; Zhan, X.Y.; Wang, Z.X.; Liu, K.L.; Safdar, M.; Sun, L.F.; He, J. A vertical-oriented WS₂ nanosheet sensitized by graphene: An advanced electrocatalyst for hydrogen evolution reaction. *Nanoscale* **2015**, *7*, 14760–14765. [[CrossRef](#)] [[PubMed](#)]
45. Yu, S.; Kim, J.; Yoon, K.R.; Jung, J.W.; Oh, J.; Kim, I.D. Rational Design of Efficient Electrocatalysts for Hydrogen Evolution Reaction: Single Layers of WS₂ Nanoplates Anchored to Hollow Nitrogen-Doped Carbon Nanofibers. *ACS Appl. Mater. Interfaces* **2015**, *7*, 28116–28121. [[CrossRef](#)] [[PubMed](#)]
46. Zou, M.L.; Chen, J.D.; Xiao, L.F.; Zhu, H.; Yang, T.T.; Zhang, M.; Du, M.L. WSe₂ and W(Se_xS_{1-x})₂ nanoflakes grown on carbon nanofibers for the electrocatalytic hydrogen evolution reaction. *J. Mater. Chem. A* **2015**, *3*, 18090–18097. [[CrossRef](#)]
47. Chang, Y.H.; Wu, F.Y.; Chen, T.Y.; Hsu, C.L.; Chen, C.H.; Wiryo, F.; Wei, K.H.; Chiang, C.Y.; Li, L.J. Three-Dimensional Molybdenum Sulfide Sponges for Electrocatalytic Water Splitting. *Small* **2014**, *10*, 895–900. [[CrossRef](#)] [[PubMed](#)]
48. Chang, Y.H.; Nikam, R.D.; Lin, C.T.; Huang, J.K.; Tseng, C.C.; Hsu, C.L.; Cheng, C.C.; Su, C.Y.; Li, L.J.; Chua, D.H.C. Enhanced Electrocatalytic Activity of MoS_x on TCNQ-Treated Electrode for Hydrogen Evolution Reaction. *ACS Appl. Mater. Interfaces* **2014**, *6*, 17679–17685. [[CrossRef](#)] [[PubMed](#)]
49. Huang, P.-C.; Shaikh, M.O.; Wang, S.-C. Structural and optoelectronic properties of alloyed Sn_xMn_{1-x}S thin films. *Adv. Powder Technol.* **2016**, *27*, 964–970. [[CrossRef](#)]



© 2018 by the authors. Licensee MDPI, Basel, Switzerland. This article is an open access article distributed under the terms and conditions of the Creative Commons Attribution (CC BY) license (<http://creativecommons.org/licenses/by/4.0/>).